Electronic Research Archive

https://www.aimspress.com/journal/era

ERA, 34(5): 2839–2867.
DOI: 10.3934/era.2026129
Received: 15 December 2025
Revised: 16 March 2026
Accepted: 25 March 2026
Published: 31 March 2026

Research article

Dynamic behaviours of flexible plates vertically fixed in a channel

Omar Aref[1,2], Li Wang[1], John Young[1] and Fang-Bao Tian[1,*]

[1] School of Engineering and Technology, University of New South Wales, Canberra, ACT 2600, Australia

[2] Computer Based Engineering Applications Department, Informatics Research Institute, City of Scientific Research and Technological Applications, New Borg El Arab City, 21934, Egypt

* **Correspondence:** Email: fangbao.tian@unsw.edu.au.

Abstract: This work studies the nonlinear dynamics of plates vertically attached to a channel using the immersed boundary-lattice Boltzmann-general interpolation material point method. The hydrodynamic flow and dynamics of the plate walls over a broad range of Reynolds numbers, structure-to-fluid mass ratio, and bending stiffness are analysed. Four modes are identified: stable plate with symmetric vortex, stable plate with asymmetric vortex, unstable plate with symmetric vortex, and unstable plate with asymmetric vortex. The modes represent distinct flow-structure interaction scenarios observed during the study of plates subjected to fluid flows. A symmetric wake remains aligned with the centreline of the artery over time, while an asymmetric wake deviates upwards or downwards from the centreline. The potential pathways to steady and unsteady behaviour are explored. The physical mechanisms that cause different modes of dynamic response for the plates are discussed.

Keywords: fluid-structure interaction; immersed boundary method; lattice Boltzmann method; channel flow; stenosis

1. Introduction

Chronic venous disease (CVD) is one of the most prevalent disorders of the vascular system worldwide and significantly diminishes the quality of life for millions of individuals. The primary cause of CVD occurs owing to dysfunction of the venous valves (VV) within veins, resulting in back blood flow (venous reflux) when the valves fail to close completely (incompetent). Both the retrograde flow of venous blood and the resultant increased venous pressure result in blood pooling in the lower extremities and other pathological processes associated with this disease as a result of venous hypertension, such as the development of varicose veins, edema, skin changes, and the formation of venous ulcers [1, 2]. Therefore, it is essential to study the dynamic properties of the

dysfunctional venous valves in order to identify the factors leading to valve malfunction and venous disease progression.

Obtaining an accurate identification of the mechanisms involved in valve incompetence is a complex process, posing challenges on the surgeries [3]. To study this, a simplified geometry of the valve has been created to analyse the dynamic interaction of the leaflets with the blood. Fluid-structure interaction (FSI) simulation provides an accurate representation of blood flow through flexible veins and venous valves, providing a strong foundation for the diagnosis and monitoring of the disease [4]. Results obtained using an FSI approach give a more accurate representation of the valve region. By taking into account that the material characteristics of the leaflets are thin and flexible, the FSI approach provides more reliable results when looking at the valve region compared to a rigid wall method [5]. The flow characteristics (i.e., how the blood is flowing) and critical pressures (i.e., where pressure drop occurs) affect the behaviour of the flow in relation to how open the valve is and if there is a leakage gap in the valve. As a result, the FSI approach is strongly recommended when assessing blood flow through a dysfunctional venous valve [6]. FSI modeling has a very different impact on both deformation and gap than does the rigid-wall model. These differences in deformation and gap create substantial differences in the resulting pressure drop and magnitude of the reflux jet. As such, accurate simulation of blood flow through dysfunctional venous valves is needed [7].

There are a few methods to provide FSI modeling (see e.g., [8–10]). Among these methods, the partitioned FSI coupling is very convenient, as fluid and structure dynamics are solved in a separated way, and are coupled through boundary conditions. Therefore, researchers can use any methods for either fluid or structure dynamics. For flows involving complex geometries and moving boundaries, the immersed boundary-lattice Boltzmann method (IB-LBM) combined with the structure solvers has attracted growing attention in the past few years [7, 10]. The immersed boundary method (IBM) is very convenient in terms of mesh generation and treatment, while the lattice Boltzmann method (LBM) is efficient in modeling unsteady flows [11, 12]. The IB-LBM has the ability to examine the phenomena associated with different forms of fluid-structure interactions modes, which involve the unsteady forces exerted by the flow on the structure and time-varying behavior on structures affecting the flow. This process shares similar physics for biological systems. Particularly, the unsteady flow dynamics is experienced by VV structures during periods of pulsatile flow, while the VV deformation impacts the blood vessel flows [13]. A comprehensive study of feedback IB-LBM, with particular emphasis on velocity penetration within immersed boundary and their consequences on blood flow simulation involving flexible plate was conducted which enhanced understanding this treatment for accurate predictions of blood flow [7]. Combining IBM and LBM allows the modeling of fluid structure interactions, allowing numerically validations and creating treatment options based on the results of fluid dynamics studies conducted in stenosed arteries, and therefore creating a profound impact on clinical practice in the future of cardiovascular medicine [14]. Therefore, the IB-LBM could provide accurate outcomes regarding the immersed structure even when subjected to large deformations [15], enabling researchers to develop realistic simulations of the dynamics behavour of blood flow inside blood vessel (BV) [15].

For structure solvers, the general interpolation material point method (GIMPM) demonstrates excellent performance in modeling structural dynamics involving large deformations and complex interactions with various materials. The GIMPM analyzes the solid particles properties in detail under different conditions for BV walls with varying flow conditions which provides great flexibility

in simulating complex systems as considered in this work [16, 17]. Recently, this GIMPM was incorporated with the IB-LBM to conduct FSI of collapsible channels, demonstrating its capability in modeling similar systems [18]. Therefore, this work will employ the IB-LBM-GIMPM to model the simplified dynamic system.

Extensive investigations [19–21] have been conducted to study the interaction between the flow and the flexible walls (a simplified representation of venous valves) using various arrangements in a viscous flow. Previous studies have been primarily conducted on rigid walls [22,23] to investigate flow patterns. Recently, a greater focus has been on studying the flow characteristics and uncovering the process behind vortex modes and vibration transitions inside the VV [10,24]. Here, this work focuses on the dynamic behaviours of flexible plates vertically fixed in a channel as a simplified model of the diseased VV.

There contribution of this work includes three aspects. First, this study presents a stability map that defines the instability boundaries for this specific configuration. This is a diagram which has not been previously published for this application. Second, this study identifies four unique modes of FSI behavior that have not been previously identified for this application. Furthermore, the use of one-sided and two-sided FSI comparisons indicates that adding a second plate produces a significant reduction in the critical Reynolds number due to the increased number of coupling modes between the two plates. This result aligns with the findings that tandem arrangements significantly amplify flow-induced vibration (VIV) and alter the stability boundaries of coupled systems as opposed to single configurations. Third, this study links the dynamics of FSI to the dysfunction of venous valves through the relationships between pressure distributions and WSS distributions and failure of valves. These results provide support for the findings of Bergan et al. [25], who found that abnormal haemodynamic forces initiate the inflammatory processes resulting in chronic venous disease.

The remaining of this work is arranged as follows: Section 2 introduces the physical model and numerical method; the results are discussion in Section 3; and the conclusion marks are given in Section 4.

2. Physical model and numerical method

2.1. Physical model and governing equations

A 2D incompressible flow over flexible plates vertically fixed in a channel is considered, as shown in Figure 1. The vertical plates serves as an idealised model to study the dynamic system with significantly reduced computational cost. The length of the plate is $L_{ref} = 1.0$. The channel is $D = 2.5L_{ref}$ in diameter. A Poiseuille flow with an average velocity of U_o is imposed at the inlet of the channel, and a constant pressure p_d is specified at the outlet. To eliminate the pressure drop effect on the results, the average pressure P_{av} is calculated over the dashed line.

Two configurations, a one-sided and two-sided model, are examined (see Figure 1). The one-sided configuration acts as a baseline against which the plate-to-plate hydrodynamic coupling effect can be assessed. The comparison of identical conditions for both configurations provides a measure of the destabilising effect of multi-body interaction. The physical model is scientifically justified for the following reasons namely: geometric analogy, physical prospective and parameter regime. Regarding geometric analogy, the VV's thin, flexible leaflets (cusps) project vertically into the vessel lumen and are anchored at their base to the wall of the vein. When the leaflets are not functioning

properly, they do not coapt appropriately, and the shape resembles two flexible plates or leaflets that are anchored vertically in a channel. By using ultrasound imaging, Lurie et al. [26] demonstrated that vortex formation in the sinus of the valve is the mechanism closing the valves. In addition, the dynamic interaction between the leaflet flexibility, retrograde flow, and the vortex structures together determines the competence of the valve, which is analogous to the FSI modes demonstrated in the previous simulations. Buxton and Clarke [27] confirmed that a plate/leaflet-in-channel model is a valid representation of the mechanics of the venous valve. Regarding physical relevance, the main phenomena observed in experiments include flow-induced oscillations, transitions from symmetric to asymmetric wake, the stability of the structure, and how it relates to mass and stiffness ratios. These phenomena have direct relevance for studying how planar venous valve leaflets respond to retrograde blood flow. Fluttering-incompetent venous valves demonstrate oscillatory behaviours, and the shift from stable to unstably dynamic directly affect the ability of the valve to completely close (preventing venous reflux). Tien et al. [28] reported that all bioprosthetic valve leaflet behaviours were controlled through FSI mechanisms as measured in this study. There is further evidence linking increased venous pressure to inflammation occurring within the venous valve in a manner that alters the stiffness of the valve leaflet, which further supports how structural properties can affect the functioning of the valve linearly, as was quantified by Takase et al. [29]. Regarding parameter regime, the range of Reynolds numbers (Re) studied in this work is $Re = 25$ - 600, which corresponds approximately to the conditions associated with blood running through veins. In [30], it was suggested that venous flow has Reynolds numbers, on average, ranging from approximately $Re \approx 50$ in smaller veins (including superficial veins) to approximately $Re \approx 470 \pm 144$ in the resting inferior vena cava, and increasing to approximately $Re \approx 589 \pm 205$ when a person exercises. Since all of these values fall well within the range of values studied in our parametric analysis, the results presented in this work certainly has physiological significance.

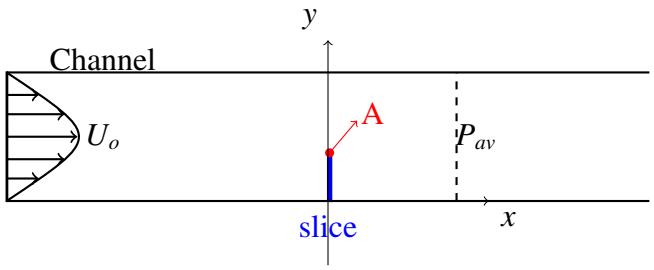

(a) One-sided model.

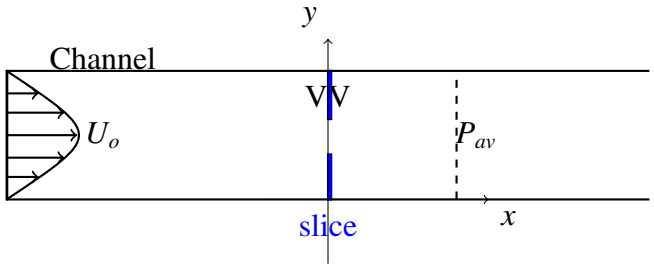

(b) Two-sided model.

Figure 1. Schematic diagram of fluid flow through the flexible venous valve wall: (a) one-sided model, (b) two-sided model.

The governing equations for the fluid flow are the incompressible Navier-Stokes equations:

$$\nabla \cdot \boldsymbol{u} = 0, \qquad \rho\left(\frac{\partial \boldsymbol{u}}{\partial t} + \boldsymbol{u} \cdot \nabla \boldsymbol{u}\right) = -\nabla p + \mu \nabla^2 \boldsymbol{u} + \rho \boldsymbol{f}, \tag{2.1}$$

where ρ is the fluid density, $\boldsymbol{u}$ is velocity field, μ is the dynamic viscosity of the fluid, and $\boldsymbol{f}$ is external forces including the force introduced by the immersed boundary method.

The structure dynamics is governed by the weak form of the momentum equation in current spatial configuration [31],

$$\int_{\Omega^s} \rho^s \ddot{d}_i^s \delta d_i^s \, dV^s + \int_{\Omega^s} \sigma_{ij}^s \delta d_{i,j}^s \, dV^s - \int_{\Omega^s} \rho^s b_i^s \delta d_i^s \, dV^s - \int_{\Gamma_t^s} \bar{t}_i^s \delta d_i^s \, dA^s = 0, \tag{2.2}$$

where all variables are in the deformed configuration, Ω^s is the current (deformed) spatial configuration of the solid domain, ρ^s is the continuum structure density, $\ddot{d}_i^s$ is the acceleration of the solid, d_i^s is the displacement, dV^s is the infinitesimal volume element in the current configuration, σ_{ij}^s is the Cauchy stress tensor, $\delta d_{i,j}^s = \frac{\partial \delta d_i^s}{\partial x_j}$ is the spatial gradient of the virtual displacement, b_i^s are external forces acting on the solid, Γ_t^s is the traction boundary, $\bar{t}_i^s$ is the surface traction, and dA^s is the infinitesimal area element. The superscript $()^s$ indicates that corresponding quantities belong to the structure. Two material models are explored here: the isotropic elastic model and the hyper-elastic Neo-Hookean model. The isotropic elastic material is described by the following equation [31]:

$$\frac{\partial \sigma_{ij}^s}{\partial t^s} = \frac{1}{2} C_{ijkl}^s \left(\frac{\partial \dot{d}_l}{\partial x_k} + \frac{\partial \dot{d}_k^s}{\partial x_l}\right) + \sigma_{ik}^s \dot{\omega}_{jk}^s + \sigma_{jk}^s \dot{\omega}_{ik}^s, \tag{2.3}$$

where C_{ijkl}^s denotes the components of the elasticity tensor that relate stresses to strains in the material, and $\dot{d}_l$, $\dot{d}_k$ are respectively the velocity field components in the directions l and k, and ω_{ij}^s is the vorticity tensor defined as,

$$\omega_{ij}^s = \frac{1}{2}\left(\frac{\partial \dot{d}_j}{\partial x_i} - \frac{\partial \dot{d}_i}{\partial x_j}\right). \tag{2.4}$$

For the hyper elastic material model, The following equations are used to evaluate first Piola-Kirchhoff stress and Cauchy stress tensors [31]:

$$\boldsymbol{P^s} = \lambda^s \ln J \boldsymbol{F_s}^{-1} + \mu^s \boldsymbol{F_s}^{-1}\left(\boldsymbol{F_s}\boldsymbol{F_s}^T - \boldsymbol{I}\right), \tag{2.5}$$

$$\boldsymbol{\sigma_{ij}^s} = \frac{\lambda^s ln J}{J}\boldsymbol{I} + \frac{\mu^s}{J}\left(\boldsymbol{F_s}\boldsymbol{F_s}^T - \boldsymbol{I}\right), \tag{2.6}$$

where $\boldsymbol{P}^s$ is the first Piola-Kirchhoff stress tensor, $\boldsymbol{F}^s = \boldsymbol{I} + \frac{\partial \boldsymbol{d}}{\partial \boldsymbol{X}}$ is the deformation gradient tensor, $\boldsymbol{X}$ is the position vector in the initial (reference) configuration, $J = \det(\boldsymbol{F}^s)$ is the Jacobian determinant of the deformation gradient, λ^s is the first Lamé constant, μ^s is the shear modulus (second Lamé constant), and $\boldsymbol{I}$ is the second-order identity tensor.

Three non-dimensional parameters govern the system: the Reynolds number (Re), the mass ratio (M), and the bending stiffness (K_b),

$$Re = \frac{\rho U_o L_{ref}}{\mu}, \quad M = \frac{\rho^s h}{\rho L_{ref}}, \quad K_b = \frac{E h^3}{12 \rho U_o^2 L_{ref}^3}, \tag{2.7}$$

where h is the plate thickness, L_{ref} is the length of the plate and E is the Young's modulus of the plate material. Here $h = 0.1L_{\text{ref}}$. A no-slip boundary condition is applied along the plate and the channel walls. A clamped condition is used at the base of the elastic plate. The computational domain is a rectangular domain of $(-5.0\,L_{ref}, 20.0\,L_{ref})$ in x-direction and $(-0.2\,L_{ref}, 2.7\,L_{ref})$ in y-direction.

2.2. Numerical methods

The FSI system is solved by the IB-LBM-GIPMPM which includes the LBM for fluid dynamics, GIPMPM for structure dynamics and IBM for handling boundary conditions at the fluid-structure interface.

The LBM uses a fixed Eulerian grid to represent the computational domain. In this method, the fluid is simulated as a group of particles that undergo streaming and collision processes. The behaviour of fluid in the LBM is determined by the statistical properties of the distribution function, $g_i(\boldsymbol{x}, t)$. The discrete lattice Boltzmann equation of multi-relaxation time (MRT) model is used to model the fluid dynamics [32],

$$g_i(\boldsymbol{x} + \boldsymbol{e}_i\Delta t, t + \Delta t) - g_i(\boldsymbol{x}, t) = \Omega_i(\boldsymbol{x}, t) + \Delta t G_i, \tag{2.8}$$

$$\Omega_i = -(M^{-1}S\,M)_{ij}(g_j(\boldsymbol{x}, t) - g_j^{eq}(\boldsymbol{x}, t)), \tag{2.9}$$

where t is the time, $\boldsymbol{x}$ is the position of the fluid parcel, $\boldsymbol{e}_i$ is the discrete velocity in the ith direction, Δt is the time step, g_i^{eq} is the equilibrium distribution function, F_i represents the contribution of body forces, $\Omega_i(\boldsymbol{x}, t)$ is the collision operator, G_i is the contribution of the body forces , M is the transformation matrix, and S is a non-negative diagonal relaxation matrix. S can be written as,

$$S = \text{diag}(0, s_2, s_2, 0, s_4, 0, s_4, s_9, s_9), \tag{2.10}$$

where s_i are relaxation parameters. More details of S and $\boldsymbol{e_i}$ can be found in [33]. The equilibrium distribution function g_i^{eq} can be determined by

$$g_i^{eq} = \rho w_i \left[1 + \frac{\boldsymbol{e}_i \cdot \boldsymbol{u}}{c_s^2} + \frac{(\boldsymbol{e}_i \cdot \boldsymbol{u})^2}{2c_s^4} - \frac{\boldsymbol{u} \cdot \boldsymbol{u}}{2c_s^2}\right], \tag{2.11}$$

where w_i are the lattice weights, and c_s is the lattice speed of sound calculated as $\Delta x/\sqrt{3\Delta t}$ with Δx being the lattice spacing and Δt being the time step. The force terms F_i and G_i are determined by [34]

$$F_i = \left(1 - \frac{1}{2\tau}\right)\left[\boldsymbol{e}_i - \boldsymbol{u} + \frac{\boldsymbol{e}_i \cdot \boldsymbol{u}}{c_s^2}\boldsymbol{e}_i\right] \cdot \boldsymbol{f}, \quad G_i = \left[M^{-1}\left(I - \frac{S}{2}\right)M\right]_{ij} F_j. \tag{2.12}$$

The flow quantities $\boldsymbol{u}$, ρ, and p can be determined using the following equations:

$$\rho = \sum_i g_i, \quad p = \rho c_s^2, \quad \rho\boldsymbol{u} = \left(\sum_i \boldsymbol{e}_i g_i + \frac{1}{2}\Delta t \boldsymbol{f}\right). \tag{2.13}$$

For structure solver, the GIMPM is used due to combining the benefits of both Lagrangian and Eulerian approaches. In this method, the structure is discretised into material points (Lagrangian grid) which carry the mechanical properties. The data on Lagrangian points are interpolated to an Eulerian grid. Then the momentum equation is solved on the Eulerian mesh. The updated position and velocities

are interpolated back to update the quantities for the material points (MPs) on the Lagrangian grid. The nodal accelerations $\boldsymbol{a}_n$ and velocities $\boldsymbol{v}_n$ are updated according to,

$$\boldsymbol{a}_n^{t+\Delta t} = m_n^{-1}(\boldsymbol{f}_n^e - \boldsymbol{f}_n^i), \quad \boldsymbol{v}_n^{t+\Delta t} = m_n^{-1}\boldsymbol{p}_n + \Delta t \boldsymbol{a}_n^{t+\Delta t}, \tag{2.14}$$

where $\boldsymbol{f}_n^e$ and $\boldsymbol{f}_n^i$ are the nodal forces due to the elastic deformation and inertia of the structure, $\boldsymbol{p}_n$ is the nodal momentum, and m_n is the nodal mass. The material point velocity, $\dot{\boldsymbol{d}}_p$ and position $\boldsymbol{x}_p$, are determined by interpolating the solution of the updated nodal accelerations and velocities, according to

$$\dot{\boldsymbol{d}}_p^{(t+\Delta t)} = \dot{\boldsymbol{d}}_p^t + \Delta t \sum_{p\in n} S_n(\boldsymbol{x_p})\boldsymbol{a}_n^{(t+\Delta t)}, \quad \boldsymbol{x}_p^{(t+\Delta t)} = \boldsymbol{x}_p^t + \Delta t \sum_{p\in n} S_n(\boldsymbol{x_p})\boldsymbol{v}_n^{(t+\Delta t)}, \tag{2.15}$$

where S_n is the GIMPM basis function.

As the present work will address internal flow, the force on the immersed wall must be calculated using fluid stresses. To process this, the fluid stress tensor along the fluid-structure interface is first calculated,

$$\sigma = -pI + \mu\left(\nabla \boldsymbol{u} + (\nabla \boldsymbol{u})^T\right), \tag{2.16}$$

where σ is the stress tensor, and I is the identity matrix. The stress along the boundary is determined by

$$\boldsymbol{F}(s,t) = -\sigma \cdot \boldsymbol{n}, \tag{2.17}$$

where $\boldsymbol{F}$ is the force on the boundary, and $\boldsymbol{n}$ is the unit normal to the boundary which pointing into the fluid.

The IBM, initially proposed by [35], has been expanded to many applications due to its convenience in handling complicated geometries and large deformations [11, 36–40]. There are a few different versions of IBM, such as sharp-interface and diffusion-interface methods [11, 37, 41, 42]. Here the feed-back diffusion IBM is used, which implements the non-slip boundary conditions by spreading the interaction force along the fluid-structure interface onto the fluid nodes around the boundary according to,

$$\boldsymbol{f}(\boldsymbol{x},t) = -\int_\Gamma \boldsymbol{F_{ib}}(s,t)\delta(\boldsymbol{x} - \boldsymbol{X}(s,t))d\boldsymbol{s}, \tag{2.18}$$

where $\boldsymbol{f}$ is the body force, $\boldsymbol{F_{ib}}$ is the Lagrangian force (or interaction force) along the fluid-structure interface, $\boldsymbol{s}$ is the material coordinate, and δ is the Dirac delta function [36]. Here, the feedback law [11, 43] is used to determine the Lagrangian force,

$$\boldsymbol{F_{ib}}(\boldsymbol{s},t) = -\int_0^t \alpha(\boldsymbol{U_{ib}} - \boldsymbol{U})dt - \beta(\boldsymbol{U_{ib}} - \boldsymbol{U}), \tag{2.19}$$

where α and β are respectively the spring and the damping parameters, $\boldsymbol{U_{ib}}$ is the interpolated velocity based on the fluid around the boundary, and $\boldsymbol{U}$ is the structure surface velocity. $\boldsymbol{U_{ib}}$ is interpolated by

$$\boldsymbol{U_{ib}}(\boldsymbol{s},t) = \int_{\Omega_f} \boldsymbol{u}(\boldsymbol{x},t)\delta(\boldsymbol{x} - \boldsymbol{X}(s,t))d\boldsymbol{x}, \tag{2.20}$$

where $\boldsymbol{u}$ is the fluid velocity field. In order to facilitate the spreading (2.18) and interpolation (2.20), a smoothed Dirac function is used [36]. It is important to use values of α and β to achieve reliable simulations. Details of the IBM and the choice of the parameters can be found in [7].

There are differences between internal structural dynamics (as handled by GIMPM material points) and fluid-structure communication (as handled by IBM Lagrangian points). In GIMPM, material points are volumetric integration points used to discretise the solid volume inside the domain. Each material point is capable of carrying the entire range of mechanical state variables, which include the mass, velocity, stress tensor, strain, deformation gradient, and material properties (density, Young's modulus, Poisson's ratio). Each material point also travels along fixed background Eulerian grid points (the MPM grid) and is used to solve the momentum equation for the solid structure (as described in Eq (2.2)). The GIMPM basis functions (denoted S_n) provide the interpolation between the material points and the MPM grid node. The material points serve to represent the continuum solid mechanics of the structure. The theoretical principles establishing the material point framework were originally proposed by Bardenhagen and Kober [44], who originally proposed the generalised interpolation framework that utilises material point domains to mitigate the amount of cell-crossing noise that is typically produced by using traditional MPM. In IBM, IB points are local markers that allow for discretizing the interface between fluid and structure (boundary) and do not store the internal stresses or material states of each marker, but merely provide a medium for enforcing the boundary conditions across the interface between fluid (represented by the lattice Boltzmann model, LBM) and structure (represented by the generalized immersed boundary method, GIMPM). Every IBM Lagrangian point has a position, velocity, and value of the Lagrangian interaction force, F_{ib}, (Eq (2.19)). The Dirac delta function (δ) governs the spreading and interpolation between IBM Lagrangian points and the fluid's (LBM lattice) Eulerian grid. The IBM Lagrangian point formulation is based on the classical immersed boundary method developed by Peskin [36], and a feedback forcing approach developed by Goldstein et al. [43] provides the kinematic and dynamic coupling between fluid-structure interactions at the fluid-structure interface.

The algorithm for the in-house GIMP-IBM-LBM solver, used for studying the nonlinear system, follows these steps:

1) Initialise the computation arrays and parameters.
2) Calculate the interpolated velocity with Eq (2.20).
3) Determine the Lagrangian force density with Eq (2.19).
4) Spread Lagrangian force density to the Eulerian fluid nodes around the immersed boundary to obtain the body force $\boldsymbol{f}$ according to Eq (2.18) to mimic the boundary condition.
5) Interpolate the internal fluid stress and evaluate the total external force exerted on the body:

$$\boldsymbol{b}_{\boldsymbol{i}}^{\boldsymbol{s}} = [-p\boldsymbol{I} + \mu(\nabla \boldsymbol{u} + (\nabla \boldsymbol{u})^T)] \cdot \boldsymbol{n} + \boldsymbol{F}_{\textbf{external.}} \tag{2.21}$$

6) Transfer fluid forces to the structure solver.
7) Compute the maximum wave speed of the material to calculate the critical time step.
8) Calculate the basis functions and derivatives and assemble the strain-displacement arrays for each material point.
9) Project the quantities of the material point (mass and momentum) to the associated nodes and solve the equations of motion explicitly.

10) Apply the boundary conditions of geometric constraints (clamped, sliding) and loads (point, distributed, surface load).

11) Interpolate nodal solutions (acceleration and velocity) to the material points.

12) Update particle volume and deformation-related quantities.

13) Predict the Cauchy stress.

14) Transfer the updated coordinates and velocity of the structure body to the fluid solver.

15) Conduct the stream process to obtain g_i.

16) Compute the macroscopic variables: ρ, $\boldsymbol{u}$, and p according to Eq (2.13).

17) Perform the collision step.

18) Repeat from step 2 for the next time-step.

2.3. Validation and mesh independence study

To validate the solver, a plate of length L_{ref} and thickness 0.05 L_{ref} vertically fixed in the channel is simulated. The plate is made of Saint Venant-Kirchhoff material with the density ratio of $\rho^s/\rho = 7.8$, the Young's modulus of $E/(\rho U_o^2) = 10^5$, and the Poisson's ratio of $v^s = 0.3$. Neither the gravity nor the damping is taken into account. In the simulation, the plate is purposefully built to be attached and wrapped by many layers of the Lagrangian points. Three sets of meshes are used in the following manner: $\Delta s/L_{ref} = 0.01, 0.005, 0.0025$. Due to the usage of a weak solid material for the plate, a substantial deformation is anticipated. The node located at the top of the plate is selected to monitor the horizontal displacement. Figure 2 displays the time history for the displacement $(x - x_o)/L_{ref}$ observed at the tip of the plate. The system reaches a steady state at around 15 t/T where $T = L_{ref}/U_0$. The results are compared with those obtained from [45] with different grid sizes. A good agreement is observed between the current results and the reference. In addition, the grid size has a slight effect on results, and such an effect is minimal when the mesh is less than 0.005. Therefore, $\Delta s/L_{ref} = 0.005$ is used in this work.

Lagrangian and Eulerian grid effects are evaluated by utilizing existing guidelines [45, 46] . In doing this, the ratio must remain between 0.5 and 1.0. This is needed to achieve a sufficient density of marker points within the immersed boundary layer, which will reduce leakage from the flow through the immersed boundary and facilitate accurate conditioning of the force spreading. The selection of the remaining IBM parameters (selected according to Huang et al.) [7]. Huang et al. IBM parameter values minimize the amount of flow that penetrates through to the immersed boundary. To further validate the spatial discretization, convergence tests were performed for three independent grid resolutions, with results showing that TIP displacement converges. Three primary reasons account for the variation between our work and that of Han et al. [45] in the initial transient period of computation ($t/T \sim 0 - 2$) shown in Figure 2, which is attributed to fundamental differences in the numerical approach as opposed to insufficient grid resolution. The primary reasons being (i) the instantaneous application of the Poiseuille flow profile (i.e., a pressure wave) which is very sensitive to the numerical scheme applied and as such generates transient pressure waves; (ii) the feedback IBM utilizes a proportional-integral controller in order to achieve an instantaneous no-slip condition thus requires

approximately 1–2 time units to establish tight velocity matching, unlike the direct forcing approach used by Han et al. [45] which enforces the boundary velocity instantaneously, resulting in a well-documented difference between IBM variants with regards to the transient behaviour of the respective methods [46]; and (iii) differences in the spatial discretisation and time integration between the GIMPM and the ELL solvers used to model the structural response lead to slightly different predictions during periods of rapid initial loading. However, despite these early time differences, the results from both methods converge at around the same deflection after $t/T \sim 10 - 15$, showing both solvers are acting on the same physical problem. Additionally, this non-conformance during the transient period does not detract from the validity of the parametric investigations conducted, since all parametric study results in Sections 3.1–3.4 were obtained at $t/T \sim 200 - 220$, after the system has reached a steady state.

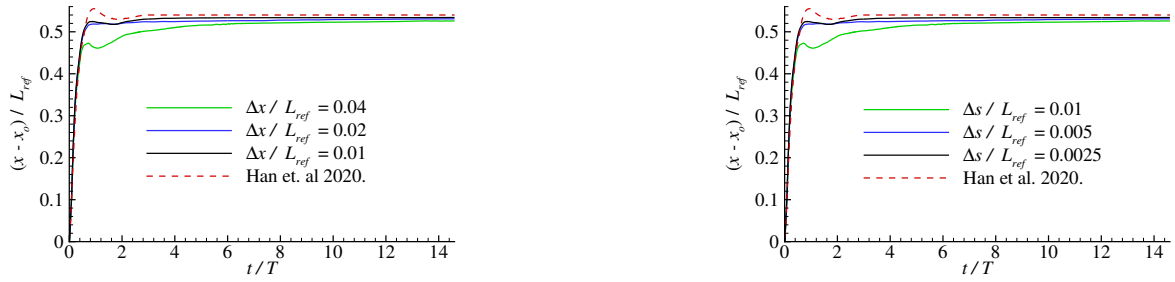

(a) Eulerian grid.

(b) Lagrangian grid.

Figure 2. Plate validation and grid convergence test for: (a) Eulerian, and (b) Lagrangian.

3. Results and discussions

In this section, the hydrodynamic flow and dynamics of the plates over a broad range of Reynolds numbers, structure-to-fluid mass ratio, and bending stiffness are analysed. The monitoring point for the plate is located at the tip of the free end (point A as indicated in Figure 1), denoted by x_o and y_o. For the two-sided case at $t = 0$: $x_o/L_{ref} = 0.0$ and $y_o/L_{ref} = 1$ for the lower plate and $x_o/L_{ref} = 0.0$ and $y_o/L_{ref} = 1.5$ for the upper plate. For the one-sided case at $t = 0$, $x_o/L_{ref} = 0.0$ and $y_o/L_{ref} = 1.0$ for the lower plate only. The time history is used to study the frequency and stability of the system.

Values of the parameters are chosen in view of existing literature and lie in the physiological range for VV flow . The critical values for Reynolds number ranges are between 50–614 [30, 47, 48]. Regarding the mechanical properties of the artery, the Young's modulus value ranges between 1.2×10^6 to 5.7×10^6 Pa [49,50]. Blood density is approximately $1.05 g/cm^3$ [51]. The Re, K_b and M values are determined based on the above introduced data.

3.1. Effect of structure-to-fluid mass ratio

To study the mass ratio effect, the bending rigidity and the Reynolds number are set as $K_b = 0.2$ and $Re = 25$, and the dynamics behaviours for $M = 1.0, 2.0, 3.0$, and 4.0 are studied. The time history of the displacement of the plate tip at $Re = 25$, $K_b = 0.2$ are shown in Figure 3. A stable state is observed for $M = 1$ as shown in Figure 3(a), while an unstable state is observed when mass ratio increased to 4 as shown in Figure 3(b). This behaviour is consistent with the behaviour observed in [52], where it

is shown that increasing the mass ratio in viscous flows correspondingly reduces the critical velocity required across the channel for the onset of instability. Similar observation was reported by Wang and Christov [53] who claimed that the unstable modes in compliant channels exhibit strong oscillatory behaviour with increasing mass ratios.

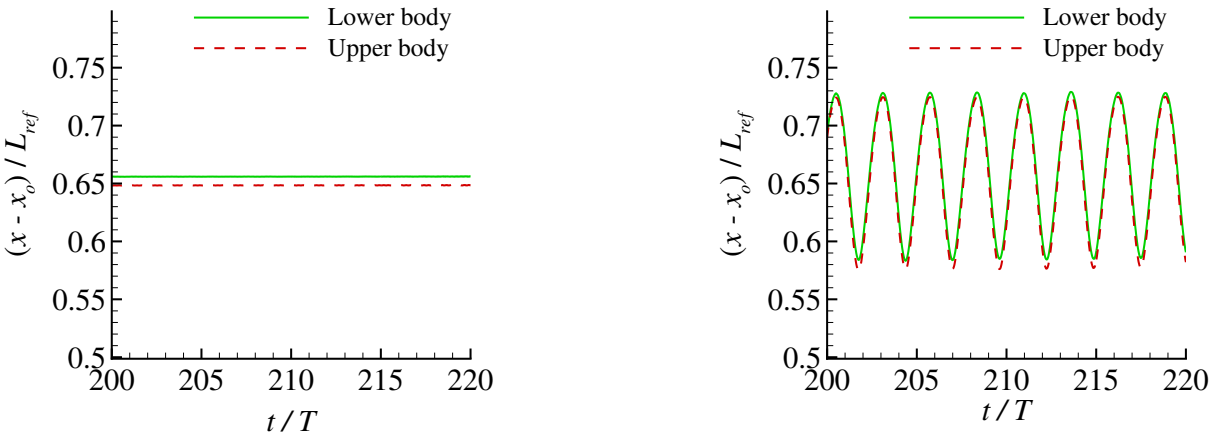

(a) $M = 1$: steady deflection.

(b) $M = 4$: unsteady deflection.

Figure 3. Time history and its PSD of the monitoring point at $Re = 25$, $K_b = 0.2$: (a) $M = 1$, and (b) $M = 4$.

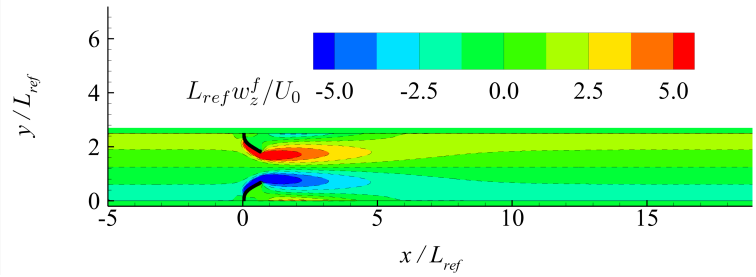

(a) $M = 1$: steady symmetric vortex structures.

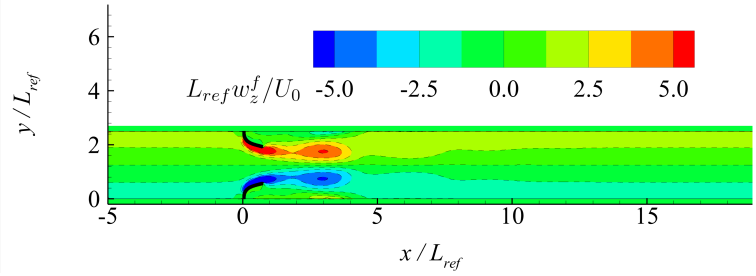

(b) $M = 4$: unsteady symmetric vortex structures.

Figure 4. Instantaneous vorticity ($L_{ref} w_z^f / U_0$) at $t/T = 200$ for $Re = 25$ and $K_b = 0.2$: (a) $M = 1$, and (b) $M = 4$.

To understand the physics behind this, fluid forces, vortex structures, and flow regimes must be evaluated. Figure 4 shows instantaneous vorticity contours ($L_{ref}w_z^f/U_0$) at $t/T = 200$ for $Re = 25$ and $K_b = 0.2$. Stable symmetric vortex structures are shown in Figure 4a, while the unstable symmetric vortex structures are shown in Figure 4b. Two major states have been identified: steady and unsteady symmetric states. In the case of a low mass ratio, such as $M = 1.0$, the plates exhibit steady behaviour. When the mass ratio increases, the plates start to vibrate, characterised by a fundamental frequency. This finding is similar to the flow-induced vibration of a flag subjected to uniform flows [54, 55]. For $M = 1$ and $M = 2$, the dominance of viscous forces leads to a stable flow pattern. For $M = 3$ and $M = 4$, the structure inertia effect becomes significant, leading to the unsteady states with two plates vibrating in phase. This unsteadiness results from increased inertial forces, which cause periodic vortex shedding while maintaining the overall symmetry. The unsteady behaviour occurs for heavier structures because of the delayed response of the structure by the dynamic forces from the surrounding fluid. The structure stores kinetic energy, which is periodically released back into the fluid. This feedback induces the unsteady oscillations. As the structure becomes heavier, this effect becomes more dominant compared to the viscous force. A similar phenomenon was observed for inverted flexible plate [56], filament [57], and flag [58].

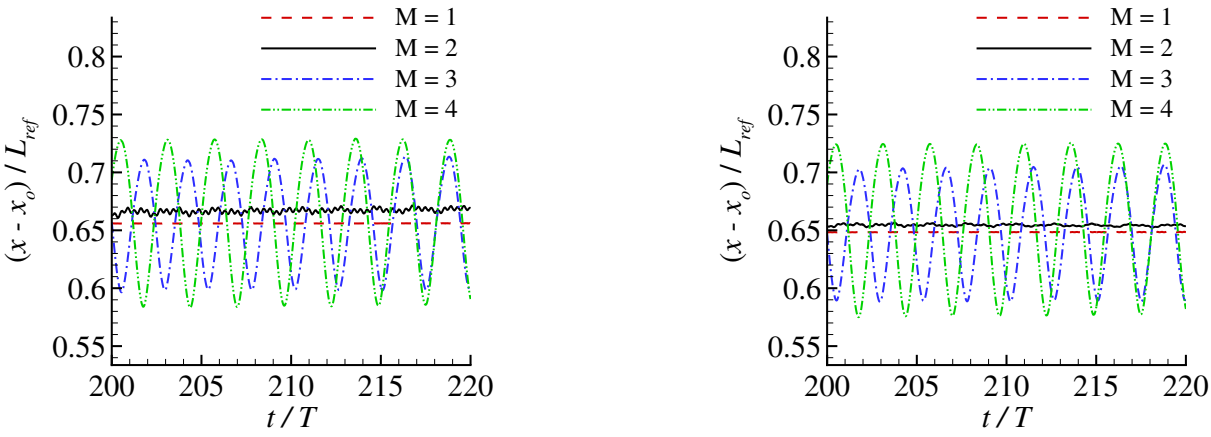

(a) Lower plate.

(b) Upper plate.

Figure 5. Deflection ($(x - x_o)/L_{ref}$) for the upper and lower plates for $Re = 25$ and $K_b = 0.2$: (a) lower plate, and (b) upper plate.

Figure 5 shows the deflection for the upper and lower plates for different mass ratios with $Re = 25$ and $K_b = 0.2$. Several observations are observed. First, both upper and lower plates have the almost same deflection. This is consistent with the symmetric feature of the flow fields discussed above. Second, the plates undergoing oscillations at higher mass ratio. Note that the Reynolds number is only 25, which is below the subcritical value under which there is no vortex shedding if the plate is rigid. However, due to the FSI, the system becomes unstable. Such phenomenon was observed for flow-induced vibrations of cylinders [59]. Third, there is a minor oscillation for $M = 2$, which is more like weak oscillation in the far field downstream. Fourth, when M increases, the oscillation amplitude of unsteady cases increases. This feature is quite similar to the convectively unstable FSI system which

requires a heavier structure to trigger the flow induced vibration [60]. Finally, the oscillation frequency decreases as M increases. This trend is similar to the relationship between the eigenvalue and the mass.

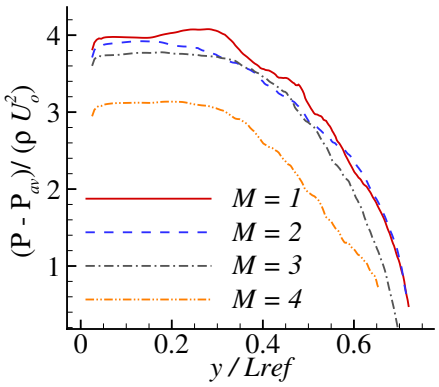

(a) Pressure along lower plate wall.

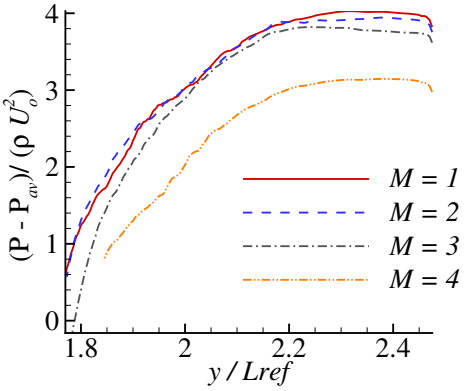

(b) Pressure along upper plate wall.

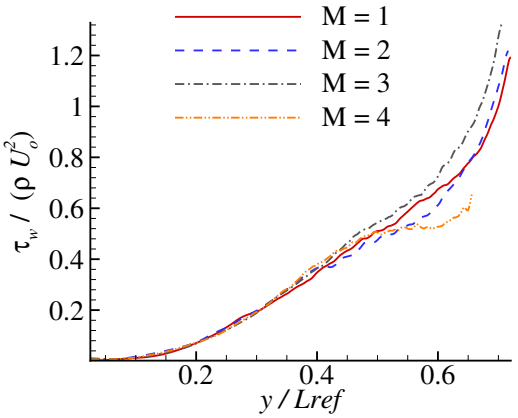

(c) WSS along lower plate wall.

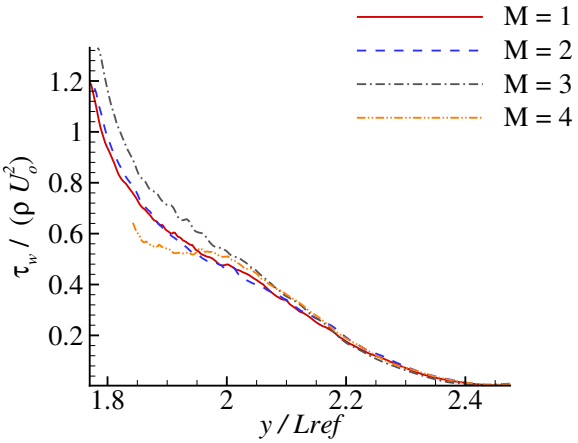

(d) WSS along upper plate wall.

Figure 6. Pressure ($(P - P_{av})/\rho U_o^2$) and WSS ($\tau_w/\rho U_o^2$) along the up stream surface for the upper and lower plate at $Re = 25$ and $K_b = 0.2$ at $t/T = 200$: (a) pressure along lower plate wall, (b) pressure along upper plate wall, (c) WSS along lower plate wall, and (d) WSS along upper plate wall. The stress is interpolated at a distance of $2.5dx$ from the fluid-structure interface.

Figure 6 shows the pressure and wall shear stress (WSS) for the upper and lower plates at $Re = 25$ and $K_b = 0.2$. It is noted that both the mechanical and biological factors are important in the biological system. Mechanical factors include WSS [61], surface pressure [62], arterial wall stiffness [63] and blood flow characteristics [64], while biological factors include endothelial dysfunction [65] and cellular composition [66]. Particularly, the WSS and the surface pressure on the VV is crucial to determining the stability of the VV and the possibility of rupture. It is noted that the surface pressure depends on the blockage ratio that happens due to oscillation. For $M = 4$, there is lower surface

pressure due to higher blockage by the plate, causing higher speed (Bernoulli's Principle). The WSS for the steady cases (e.g., $M = 1$ and 2) is nearly independent of the mass ratio; while it is affected by the mass ratio for the unsteady cases (e.g., $M = 3$ and 4), especially near the tip of the plate, indicating that the beam mass plays a major role in the unsteadiness of the system, as shown in Figures 6(c),(d). A more significant effect on pressure has been observed, even for the steady cases.

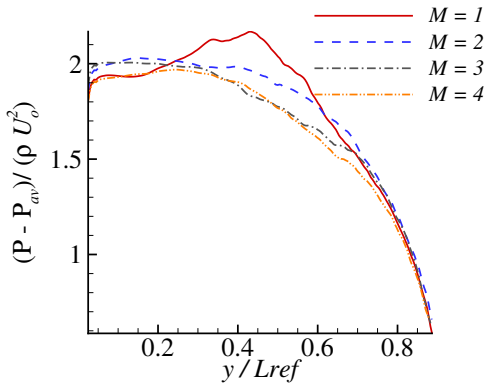

(a) Pressure ($(P - P_{av})/\rho U_o^2$) along lower plate wall.

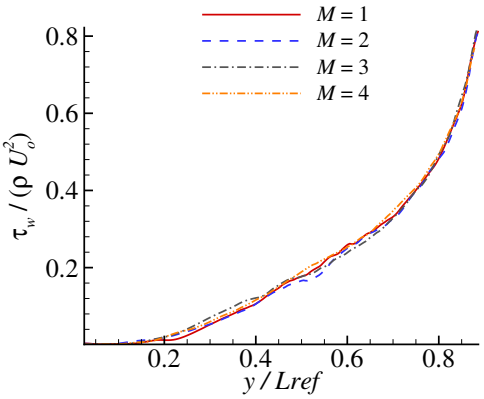

(b) WSS ($\tau_w/\rho U_o^2$) along lower plate wall.

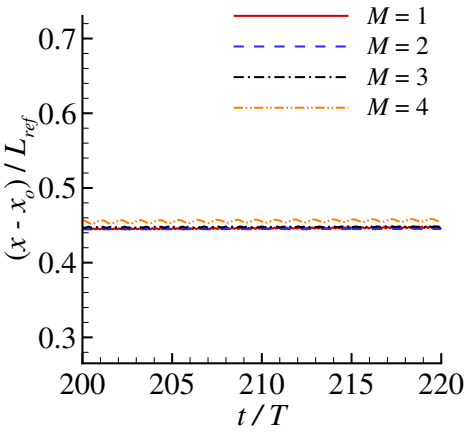

(c) Time history of $(x - x_o)/L_{ref}$ of the plate tip.

Figure 7. One-sided case, pressure, WSS (τ_w), and deflection for $Re = 25$ and $K_b = 0.2$: (a) pressure along lower plate wall, (b) WSS along lower plate wall, and (c) deflection of the plate tip.

For comparison, Figure 7 shows the pressure, WSS, and deflection of the one-sided plate. A similar observation has been identified between one-sided and two-sided cases, except for the increasing mass ratio effect. Increasing the mass ratio does not change the flow status, or affect the time history of the tip monitoring point of the plate. There is a minor oscillation when $M = 4$, but this does not cause fundamental changes to the flow. Based on this, the presence of another body destabilises the system.

For small mass ratios, the behaviour of the two-plate system is steady; however, a larger mass ratio causes oscillations and vortex shedding. It is important to note that this conclusion is specific to the current cases analysed and does not generalise to other configurations or parameter ranges.

3.2. *Effect of bending stiffness*

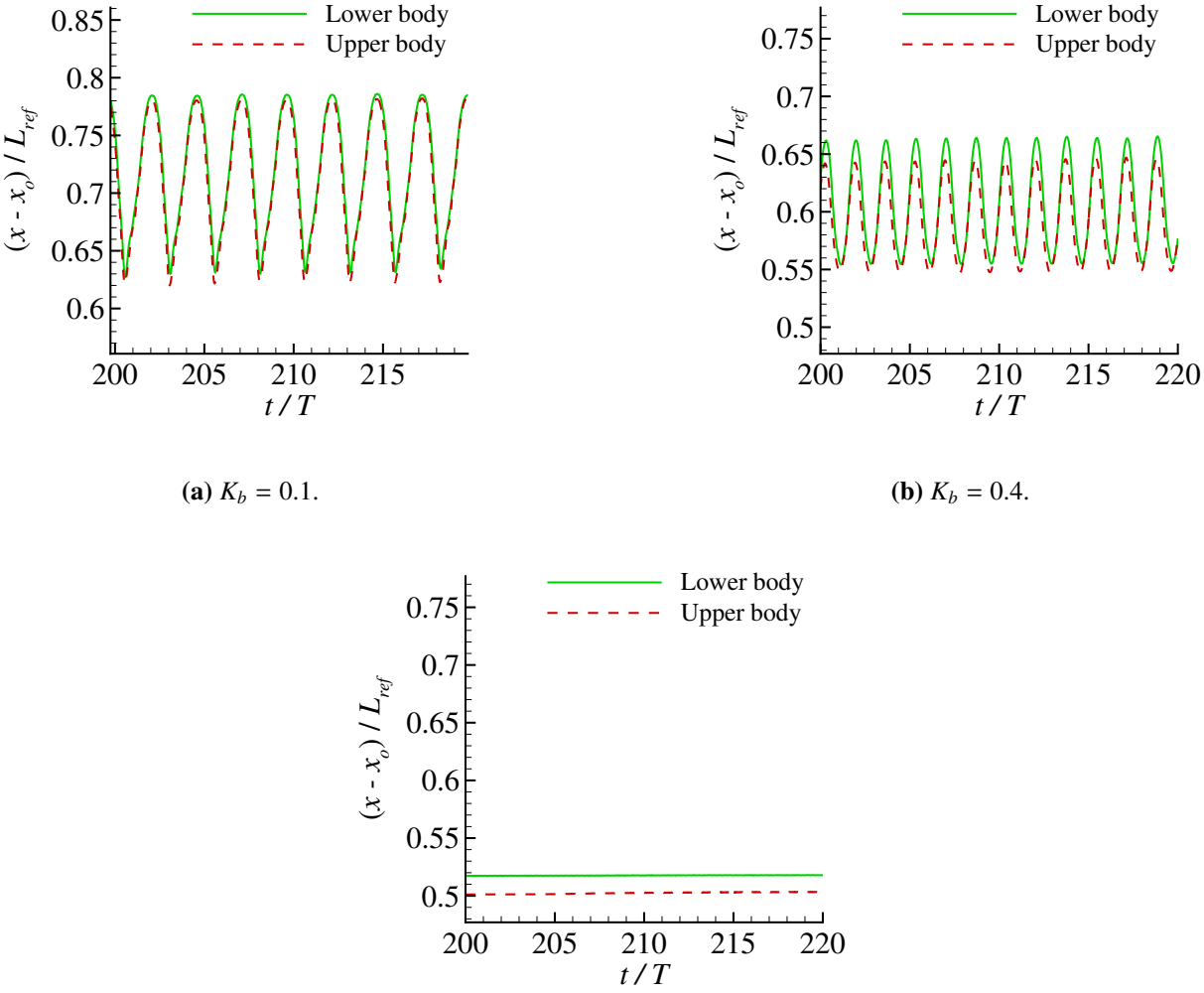

(a) $K_b = 0.1$.

(b) $K_b = 0.4$.

(c) $K_b = 0.8$.

Figure 8. Time history of the plate tip for $K_b = 0.1$ at $Re = 50$, $M = 1.0$: (a) $K_b = 0.1$, (b) $K_b = 0.4$, and (c) $K_b = 0.8$.

To study the bending rigidity effect, the mass ratio and the Reynolds number are set as $M = 1.0$ and $Re = 50$, and the dynamics behaviours are studied for $K_b = 0.1, 0.2, 0.4, 0.8$, and 1.6, as shown in Figure 8. At low bending rigidity (e.g., $K_b = 0.1$), the plates experience symmetrical unsteady behaviour; at mediate bending rigidity (e.g., $K_b = 0.2$ and 0.4), the plates undergo reduced-amplitude asymmetrical oscillations; and at high bending rigidity (e.g., $K_b = 0.8$ and 1.6), the plates are

asymmetrically steady. The present finding exhibits a disparity when compared to the phenomenon of flapping flags, in which a substantial amount of boundary layer separation serves to stabilise the flow. The observed phenomenon can be elucidated by considering the effective Reynolds number and the interaction between vortices and the wall. If a plate has lower bending rigidity, the magnitude of deformation should be more significant. However, because of the low Reynolds number in this study, the viscous force is higher than the inertial force, which resists the structure motion. The increase in bending rigidity reduces the amplitude of vibrations, subsequently leading to vibration damping. Therefore, enhancing the bending rigidity stabilises the stability of the system.

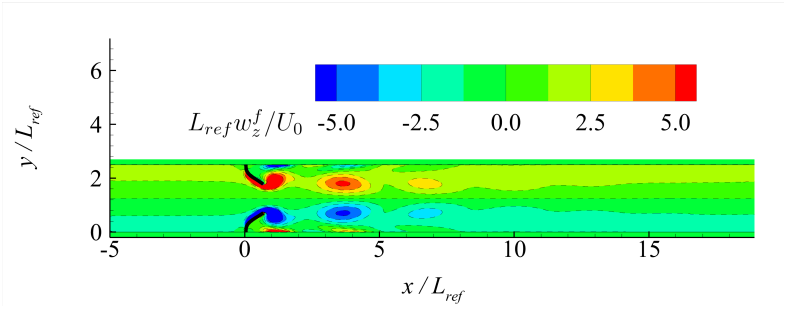

(a) $K_b = 0.1$.

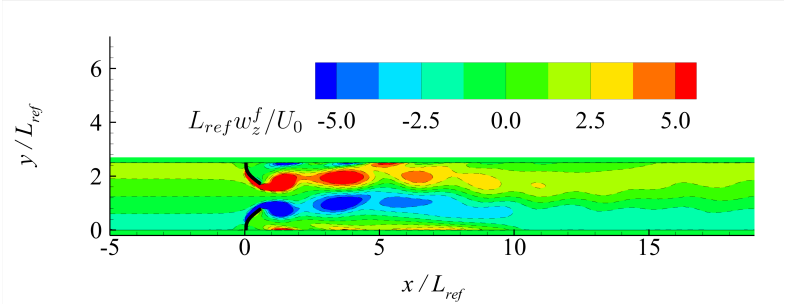

(b) $K_b = 0.4$.

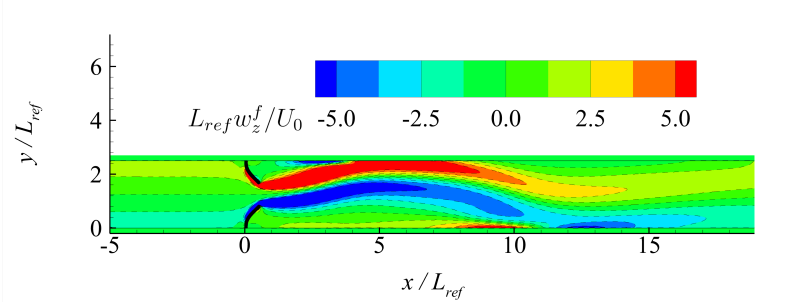

(c) $K_b = 0.8$.

Figure 9. Instantaneous vorticity contours $L_{ref}w_z^f/U_0$ at $t/T = 200$ for various K_b with $Re = 50$ and $M = 1.0$: (a)$K_b = 0.1$, (b)$K_b = 0.4$, and (c) $K_b = 0.8$.

Correspondingly, the three states can be further discussed by showing the flow fields. Instantaneous vorticity contours ($L_{ref}w_z^f/U_0$) at $t/T = 200$ are shown in Figure 9. It is clear that three different modes have been identified: unsteady symmetric vortex structures for $K_b = 0.1$, unsteady asymmetric vortex structures for $K_b = 0.4$, and steady asymmetric vortex structures for $K_b = 0.8$. The dominance of

viscous forces over inertial forces results in a stable flow pattern with an asymmetric vortex structure. An oscillation is observed due to the low value of bending rigidity. The flow pattern begins to change as the bending rigidity increases, leading to the observation of an asymmetric vortex structure. The system is forced by structure resistance to be stable at a certain value of K_b. Structural resistance refers to the increase in bending rigidity, which makes the structure more resistant to deformation.

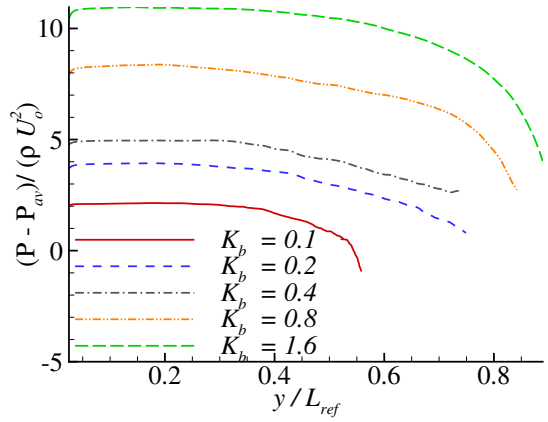

(a) Pressure $((P - P_{av})/\rho U_o^2)$ along lower plate wall.

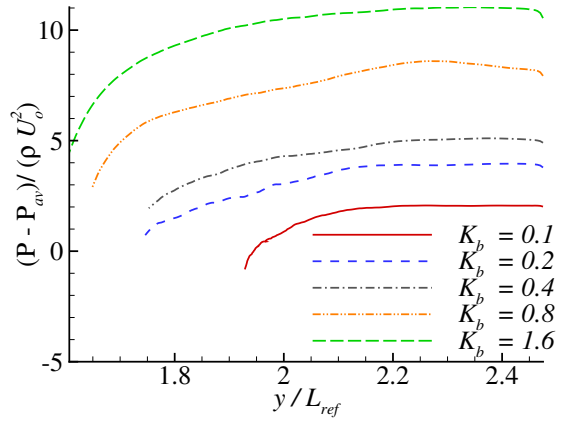

(b) Pressure $((P - P_{av})/\rho U_o^2)$ along upper plate wall.

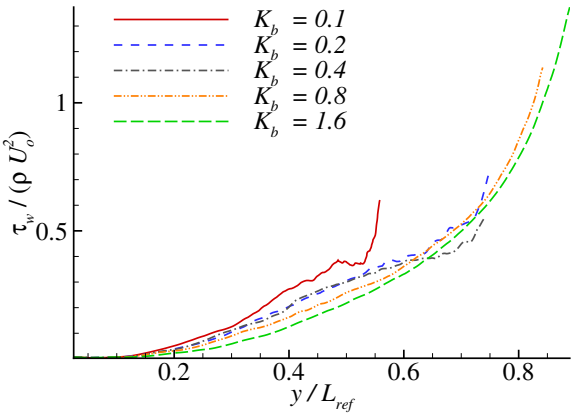

(c) WSS $(\tau_w/\rho U_o^2)$ along lower plate wall.

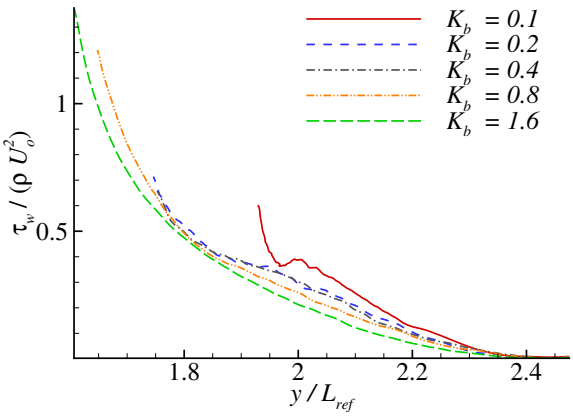

(d) WSS$(\tau_w/\rho U_o^2)$ along upper plate wall.

Figure 10. Pressure, and WSS (τ_w) for the upper and lower plate for different bending stiffness: (a) Pressure along the lower plate, (b) Pressure along the upper plate, (c) WSS along the lower plate, and (d) WSS along the upper plate.

Figure 10 shows the pressure and WSS for the upper and lower plates at $Re = 50$ and $M = 1.0$. At lower K_b, the bending rigidity does not have a significant effect on WSS due to no influence on viscous forces. To clarify this, the structure is so flexible that its bending deformation doesn't alter the fluid flow enough to affect the viscous forces acting on the wall. Literature supports this, showing that Rigid walls overestimate WSS by about 50% compared to flexible ones, underlining the severe impact of structural deformation on the WSS estimates [67]. Wall compliance is critical for determining the flow pattern and shear stress distribution [68]. The wall's bending resistance affects the flow characteristics

around it [69]. As K_b increases, the pressure along the plate surface increases due to plate resistance. As expected, the deflection decreases with increasing bending rigidity.

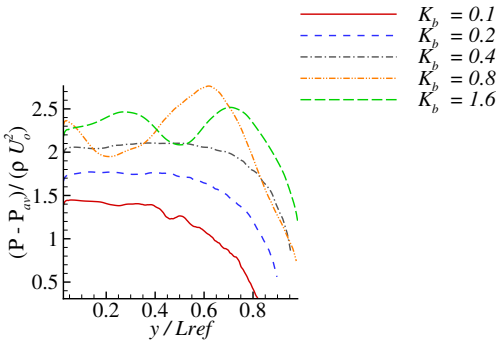

(a) Pressure ($(P - P_{av})/\rho U_o^2$) along lower plate wall.

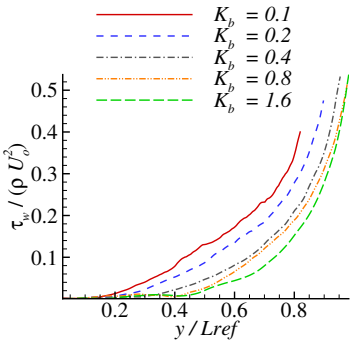

(b) WSS ($\tau_w/\rho U_o^2$) along lower plate wall.

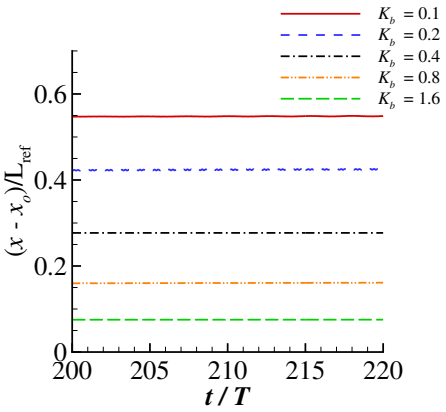

(c) The time history of the $(x - x_o)/L_{ref}$ of the monitoring point (x = 0.0 and y = 1.0 initially) at the lower elastic plate.

Figure 11. One-sided case, pressure, WSS (τ_w), and deflection for the upper and lower plate for different bending stiffness: (a) Pressure along lower plate wall, (b) WSS along lower plate wall, and (c) Deflection of lower plate free end.

For comparison, Figure 11 shows the pressure, WSS, and deflection for the lower plate for different bending rigidities of the one-sided case. A similar observation has been identified between the one-sided and two-sided cases, with the exception of the unsteady behaviour. Accordingly, the presence of another body increases the instability of the system.

3.3. Effect of Reynolds number

The mass ratio and bending rigidity are fixed with values $M = 1.0$ and $kb = 0.1$ to study the Reynolds number effect. Then the dynamics behaviours are studied for Reynolds numbers $Re = 25, 50, 100, 200, 400$, and 600. The behaviour of the thin, flexible plate in a channel is Reynolds number dependent; an increase in the Reynolds number reinforces energy transfer between the fluid and the structure, hence destabilising the FSI system [70]. Figure 12 shows the time history of the

plate tip deflection. There are three important observations. Firstly, the fluid flow exhibits a constant pattern while the plate remains stable at $Re = 25$. Secondly, as the Reynolds number increases, the plate exhibits vibrational behaviours and experiences periodic motion, particularly at high Reynolds numbers, such as $Re = 600$. Finally, the plate displays a unique vibration frequency. The interaction between the plate and the vortex at its boundary causes the plate to undergo continuous vibrations at a fundamental frequency.

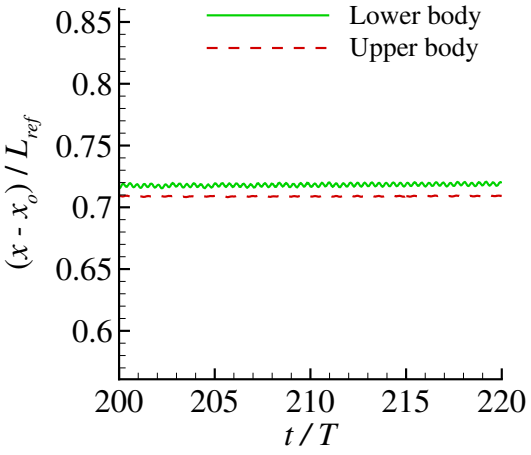

(a) $Re = 25$: deflection time history.

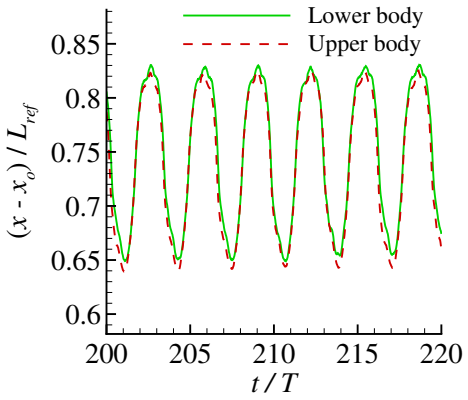

(b) $Re = 100$: deflection time history .

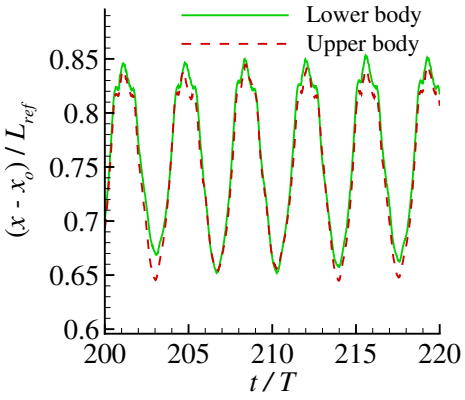

(c) $Re = 600$: deflection time history.

Figure 12. Time history and its PSD for the plate tip at $K_b = 0.1$, $M = 1.0$: (a) $Re = 25$, (b) $Re = 100$, and $Re = 600$.

Figure 13 displays the corresponding instantaneous vorticity contours of the flow field for the two-sided case. Changing Reynolds number results in three different modes: steady symmetric vortex structures for $Re = 25$ (Figure 13(a)), unsteady symmetric vortex structures for $Re = 100$ (Figure 13(b)), and unsteady asymmetric vortex structures for $Re = 200$ and $Re = 600$ (Figure 13(c)). For $Re = 25$, the dominance of viscous forces over inertial forces leads to a stable flow pattern (this

is the reason why steady symmetric vortex structures have been identified). For 50 <= Re <= 100, as the Reynolds number increases, the flow becomes unsteady, and the vortex structure oscillates. Synchronisation occurs on both plates (synchronisation means that the upper and lower plates undergo in-phase oscillations). This unsteadiness is the result of increased inertial forces, which cause periodic vortex shedding while maintaining overall symmetry. The increase in inertial forces leads to vortex shedding due to destabilised shear layers [71], and amplified flow instabilities [72]. For 200 <= Re <= 600, the dominance of inertial forces leads to complex vortex interactions and symmetry breakdown at half of the downstream. To summarize, for a small Reynolds number, the plate is stable, and the fluid flow pattern becomes steady; with an increasing value of Reynolds number, the plate starts to vibrate symmetrically; further increasing the Reynolds number leads to asymmetrical oscillations. Three different modes of vortex structure include a steady symmetric case, an unsteady symmetric case where the synchronised oscillations appear, and an unsteady asymmetric one.

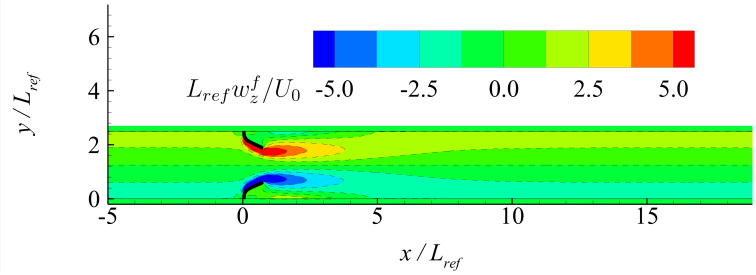

(a) Re = 25.

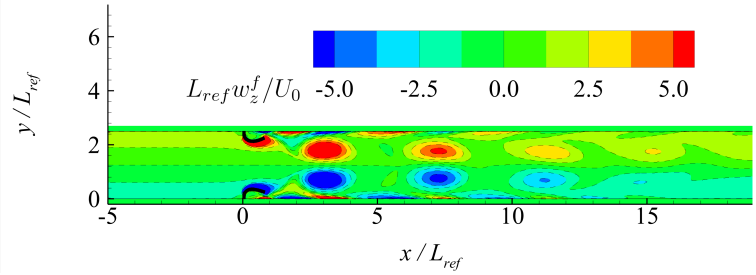

(b) Re = 100.

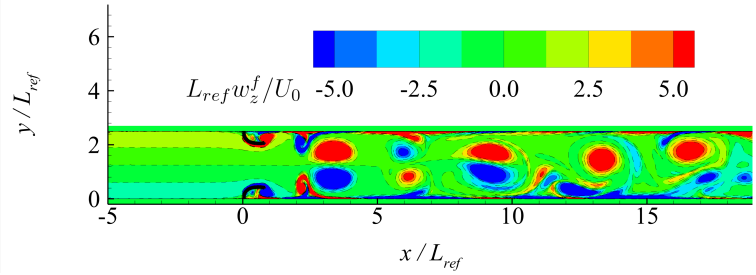

(c) Re = 600.

Figure 13. Instantaneous vorticity contours $L_{ref}w_z^f/U_0$ at t/T = 200 for K_b = 0.1 and M = 1.0: (a) Re = 25, (b) Re = 100, and (c) Re = 600.

Figure 14 shows horizontal deflection for the plate for different Reynolds numbers. Figure 14(a) shows deflection of lower plate free end in the two-sided case, while Figure 14(b) shows deflection of plate free end for one-sided case. For low *Re* fluid flows ($Re = 25$) are driven by viscous forces, causing the structure to reach near-static equilibrium (small or no oscillations). For a one-sided case, the system destabilised at $Re = 100$, while in a two-sided case, this happened at a lower $Re = 50$ due to the presence of the other plate effect. The increase in Reynolds number results in progressively stronger vortex shedding in the wake and, therefore, larger sustained periodic VIV deflections through the plates as the magnitude of the induced vibration response increases. The addition of a second plate destabilises the system and lowers the critical Reynolds number where instability exists by approximately a factor of two. This finding can only be made due to the comparison of one-sided vs. two-sided flows. This finding is physically consistent with established FSI literature. For example, Zhu and Peskin [73] showed that two interacting filaments exhibit fundamentally different dynamics from a single filament due to hydrodynamic coupling.

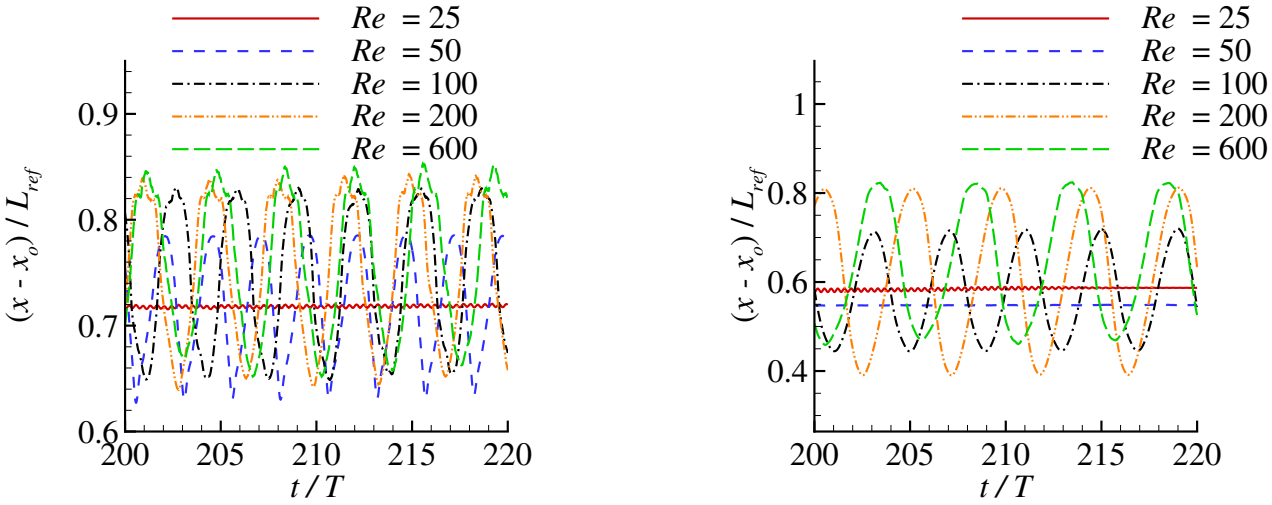

(a) The time history of the $(x - x_o)/L_{ref}$ of the monitoring point (x = 0.0 and y = 1.0 initially) at the lower elastic plate (two-sided case).

(b) The time history of the $(x - x_o)/L_{ref}$ of the monitoring point (x = 0.0 and y = 1.0 initially) at the one-sided elastic plate.

Figure 14. Deflection for the plate for different Reynolds numbers: (a) Deflection of lower plate free end (two-sided case), and (b) Deflection of plate free end (one-sided case).

Figure 15 shows the pressure, and WSS for the upper and lower plates at $M = 1$ and $K_b = 0.1$. At low *Re*, the Reynolds number has a significant effect on WSS due to the higher value of viscous forces. As *Re* increases, the fluid inertia also increases, leading to a higher pressure drop along the surface of the plate. This increase in pressure drop is primarily due to the reduction of shear stresses at the boundary layer [74]. The deflection increases with increasing Reynolds number due to strong vortex structures formed around the plate. Therefore, for an increase in the value of *Re*, the inertia of the fluid becomes much stronger compared to the viscous forces, producing sharper pressure gradients. A sharp drop in pressure with a high value of *Re* is indicative of high-speed flow and an intense adverse pressure gradient near the boundaries, creating the condition of flow separation in these regions. The

flow at low Reynolds numbers tends to be laminar, with a wall shear stress that does not change much. Ref. [75] indicated that as flow transits from laminar to turbulent, the variability in wall shear stress increases and drops more significantly at the separation point of the flow [75] . This phenomenon is further supported by studies that show how low WSS regions become less prevalent with increasing *Re* [76].

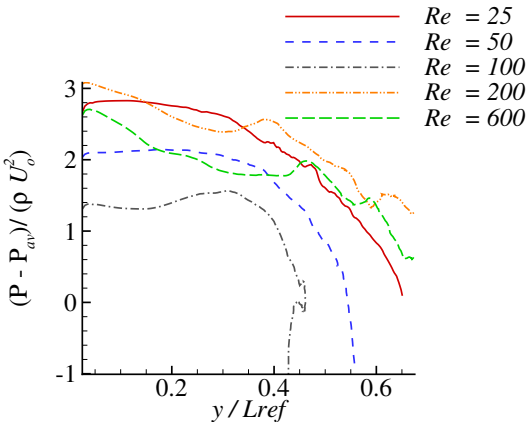

(a) Pressure $((P - P_{av})/\rho U_o^2)$ along lower plate wall.

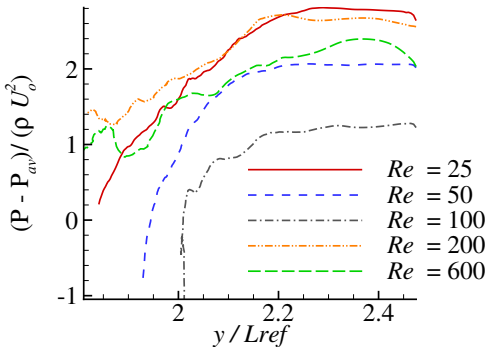

(b) Pressure $((P - P_{av})/\rho U_o^2)$ along upper plate wall.

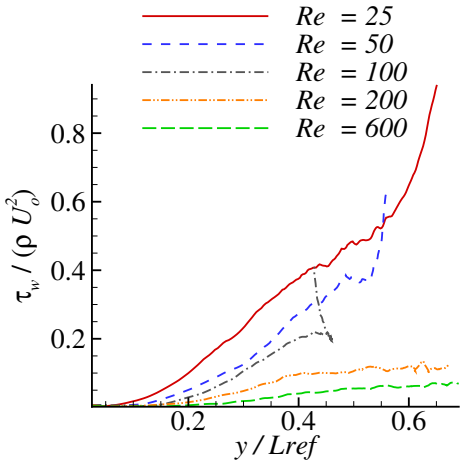

(c) WSS $(\tau_w/\rho U_o^2)$ along lower plate wall.

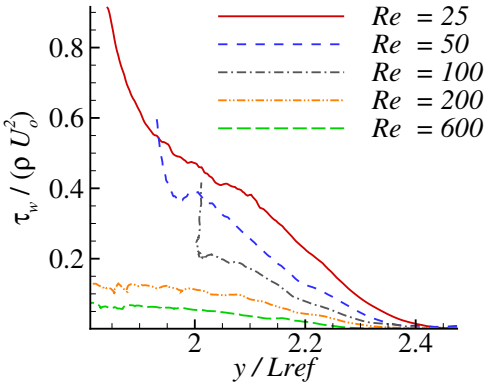

(d) WSS $(\tau_w/\rho U_o^2)$ along upper plate wall.

Figure 15. Pressure, and WSS (τ_w) for the upper and lower plate: (a) Pressure along lower plate wall, (b) Pressure along upper plate wall, (c) WSS along lower plate wall, and (d) WSS along upper plate wall.

3.4. Dynamic behaviours in the mass ratio - bending stiffness plane

To briefly discuss the dynamic behaviours in K_b-M plane, the motion state diagram in the K_b-M space is shown in Figure 16: red delta is stable; green square is unstable. Two Reynolds numbers are considered: (a) $Re = 25$; (b) $Re = 50$, which includes the transition from the stable state to the unstable state. For $Re < 25$, only a stable plate exists in the stiffness plane of the mass ratio bending.

For $Re > 50$, the plane is exclusively populated by unstable behaviours. Similar behaviour is observed. However, the persistence of another body reduces the Reynolds number required to transit to instability by half because more coupling modes occurred. According to [77], the behaviour of three filaments differs significantly from that of two filaments due to the additional coupling modes that arise. Similar phenomena exist here; more structures lead to more coupling modes.

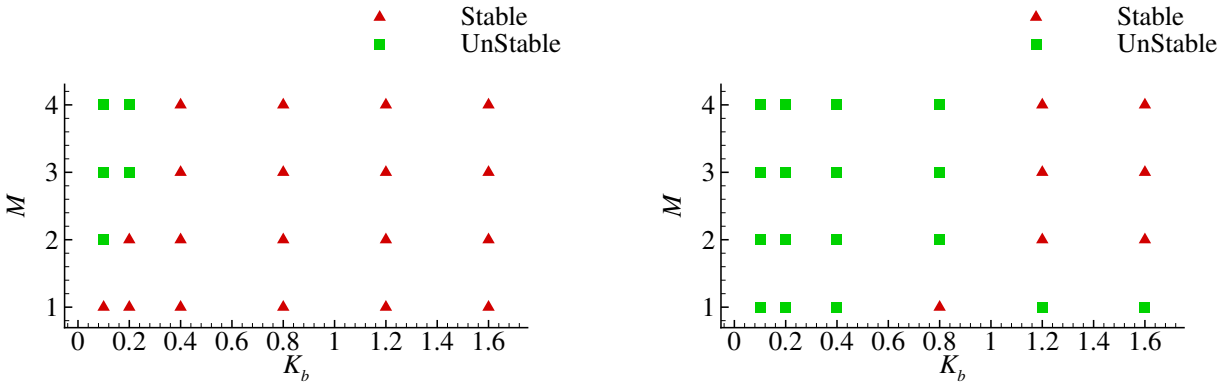

(a) $Re = 25$. **(b)** $Re = 50$.

Figure 16. Motion state diagram in the $K_b - M$ parameter space for two-sided plates: (a) $Re = 25$, and (b) $Re = 50$.

4. Conclusions

The dynamic behaviours of flexible plates vertically attached to the channel wall have been studied by varying three non-dimensional parameters: M, K_b and Re. At low mass ratios, plates exhibit steady behaviour, a vibrational behaviour characterised by a fundamental frequency as the mass ratio increases. Two modes have been identified: steady symmetric vortex structures for $M = 1$ and $M = 2$, and unsteady symmetric vortex structures for $M = 3$ and $M = 4$. At low bending rigidity, the plate initially experiences unsteady behaviour ($K_b = 0.1$), followed by low-amplitude vibration ($K_b = 0.2$ and 0.4), and turns to a steady state ($K_b = 0.8$ and 1.6). Three different modes have been identified: unsteady plate with symmetric vortex structures for $K_b = 0.1$, unsteady plate with asymmetric vortex structures for $K_b = 0.4$, and steady plate with asymmetric vortex structures for $K_b = 0.8$. The fluid flow initially follows a consistent pattern at low Reynolds numbers, and at $Re = 25$, the plate remains stable. Moreover, as the Reynolds number increases, the plate oscillates and undergoes regular movement, especially at elevated Reynolds numbers, such as $Re = 600$, resulting in a symmetry breakdown.

Use of AI tools declaration

The authors declare they have not used Artificial Intelligence (AI) tools in the creation of this article.

Acknowledgements

This work was supported by the Australian Research Council (project number DE160101098). The computation work of this research was partially performed on the National Computational

Infrastructure (NCI) supported by the Australian Government.

Conflict of interest

The authors declare there are no conflicts of interest.

References

1. M. A. Ortega, O. Fraile-Martínez, C. García-Montero, M. A. Álvarez-Mon, C. Chaowen, F. Ruiz-Grande, et al., Understanding chronic venous disease: a critical overview of its pathophysiology and medical management, *J. Clin. Med.*, **10** (2021), 3239. https://doi.org/10.3390/jcm10153239
2. S. Rațiu, M. I. Mariș, A. V. Furdui-Lința, L. V. Sima, T. I. Bratu, A. Sturza, et al., Oxidative stress in the pathophysiology of chronic venous disease: an overview, *Antioxidants*, **14** (2025), 989. https://doi.org/10.3390/antiox14080989
3. J. D. Raffetto, R. A. Khalil, Mechanisms of lower extremity vein dysfunction in chronic venous disease and implications in management of varicose veins, *Vessel Plus*, **5** (2021), 36. https://doi.org/10.20517/2574-1209.2021.16
4. M. E. Gschwandtner, H. Ehringer, Microcirculation in chronic venous insufficiency, *Vasc. Med.*, **6** (2001), 169–179. https://doi.org/10.1177/1358836x0100600308
5. Y. Zheng, H. Feng, C. He, J. Sun, Hemodynamics of asymmetrically stenotic vertebral arteries based on fluid–solid coupling, *J. Biol. Phys.*, **51** (2025), 10. https://doi.org/10.1007/s10867-025-09673-x
6. N. Rahmati, H. Pouraliakbar, A. Eskandari, K. Javari, A. Jabbarinick, P. Sadeghipour, et al., The impact of stenosis severity on hemodynamic parameters in the iliac artery: A fluid–structure interaction study, *Bioengineering*, **12** (2025), 1042. https://doi.org/10.3390/bioengineering12101042
7. Q. Huang, Z. Liu, L. Wang, S. Ravi, J. Young, J. Lai, et al., Streamline penetration, velocity error, and consequences of the feedback immersed boundary method, *Phys. Fluids*, **34** (2022), 097101. https://doi.org/10.1063/5.0101584
8. F. B. Tian, FSI modeling with the DSD/SST method for the fluid and finite difference method for the structure, *Comput. Mech.*, **54** (2014), 581–589. https://doi.org/10.1007/s00466-014-1007-3
9. F. B. Tian, Y. Wang, J. Young, J. C. S. Lai, An FSI solution technique based on the DSD/SST method and its applications, *Math. Models Methods Appl. Sci.*, **25** (2015), 2257–2285. https://doi.org/10.1142/S0218202515400084
10. Q. Huang, F. B. Tian, J. Young, J. C. Lai, Transition to chaos in a two-sided collapsible channel flow, *J. Fluid Mech.*, **926** (2021), A15. https://doi.org/10.1017/jfm.2021.710
11. W. X. Huang, F. B. Tian, Recent trends and progress in the immersed boundary method, *Proc. Inst. Mech. Eng., Part C: J. Mech. Eng. Sci.*, **233** (2019), 7617–7636. https://doi.org/10.1177/0954406219842606
12. F. B. Tian, The lattice Boltzmann method and its applications in engineering flows, *Proc. Inst. Mech. Eng., Part C: J. Mech. Eng. Sci.*, **237** (2023), 2431–2432. https://doi.org/10.1177/09544062231170105

13. A. Trotta, S. Meloni, G. Falcucci, S. Ubertini, A. Facci, An immersed boundary formulation for lattice boltzmann simulations of low-reynolds fluid–structure interaction problems, *Phys. Fluids*, **37** (2025), 034125. https://doi.org/10.1063/5.0256946

14. A. Morany, R. G. Bardon, K. Lavon, A. Hamdan, D. Bluestein, R. Haj-Ali, Analysis of fibrocalcific aortic valve stenosis: computational pre-and-post tavr haemodynamics behaviours, *R. Soc. Open Sci.*, **11** (2024), 230905. https://doi.org/10.1098/rsos.230905

15. L. Wang, D. Dong, F. B. Tian, Fast prediction of blood flow in stenosed arteries using machine learning and immersed boundary-lattice boltzmann method, *Front. Physiol.*, **13** (2022), 953702. https://doi.org/10.3389/fphys.2022.953702

16. B. Li, S. Liu, A multi-species material point method with a mixture model, *Comput. Anim. Virtual Worlds*, **35** (2024), e2239. https://doi.org/10.1002/cav.2239

17. A. G. Kuchumov, A. Makashova, S. Vladimirov, V. Borodin, A. Dokuchaeva, Fluid–structure interaction aortic valve surgery simulation: A review, *Fluids*, **8** (2023), 295. https://doi.org/10.3390/fluids8110295

18. Z. Rahimi, J. Young, F. B. Tian, Anomalous stability behaviors in two-sided wavy collapsible channels, *Phys. Fluids*, **37** (2025), 021912. https://doi.org/10.1063/5.0249541

19. Y. Li, D. Wan, D. Hu, C. Li, A novel approach for estimating blood flow dynamics factors of eccentric stenotic arteries based on ML, *Eng. Anal. Boundary Elem.*, **163** (2024), 175–185. https://doi.org/10.1016/j.enganabound.2024.03.003

20. K. Shakya, S. R. Chowdhury, A fluid–structure interaction study to analyze the severity of carotid artery stenosis at different locations and its effect on various hemodynamic biomarkers, *Eur. J. Mech. B. Fluids*, **106** (2024), 227–237. https://doi.org/10.1016/j.euromechflu.2024.04.006

21. P. G. Dake, J. Mukherjee, K. C. Sahu, A. B. Pandit, Computational fluid dynamics in cardiovascular engineering: A comprehensive review, *Trans. Indian Natl. Acad. Eng.*, **9** (2024), 335–362. https://doi.org/10.1007/s41403-024-00478-3

22. S. H. Lee, K. S. Han, N. Hur, Y. I. Cho, S. K. Jeong, The effect of patient-specific non-Newtonian blood viscosity on arterial hemodynamics predictions, *J. Mech. Med. Biol.*, **19** (2019), 1940054. https://doi.org/10.1142/S0219519419400542

23. B. M. Johnston, P. R. Johnston, S. Corney, D. Kilpatrick, Non-Newtonian blood flow in human right coronary arteries: Steady state simulations, *J. Biomech.*, **37** (2004), 709–720. https://doi.org/10.1016/j.jbiomech.2003.09.016

24. N. Sarkar, S. Roy, Periodic flow features in a planar sudden expansion with pulsatile inflow velocity, *J. Fluid Mech.*, **980** (2024), A43. https://doi.org/10.1017/jfm.2023.1074

25. J. J. Bergan, G. W. Schmid-Schönbein, P. D. C. Smith, A. N. Nicolaides, M. R. Boisseau, B. Eklof, Chronic venous disease, *N. Engl. J. Med.*, **355** (2006), 488–498. https://doi.org/10.1056/NEJMra055289

26. F. Lurie, R. L. Kistner, B. Eklof, D. Kessler, Mechanism of venous valve closure and role of the valve in circulation: a new concept, *J. Vasc. Surg.*, **38** (2003), 955–961. https://doi.org/10.1016/S0741-5214(03)00711-0

27. G. A. Buxton, N. Clarke, Computational phlebology: the simulation of a vein valve, *J. Biol. Phys.*, **32** (2006), 507–521. https://doi.org/10.1007/s10867-007-9033-4

28. W. H. Tien, H. Chen, Z. Berwick, J. Krieger, S. Chambers, D. Dabiri, et al., Characterization of a bioprosthetic bicuspid venous valve hemodynamics: implications for mechanism of valve dynamics, *Eur. J. Vasc. Endovasc. Surg.*, **48** (2014), 459–464. https://doi.org/10.1016/j.ejvs.2014.06.034

29. S. Takase, L. Pascarella, L. Lerond, J. Bergan, G. Schmid-Schönbein, Venous hypertension, inflammation and valve remodeling, *Eur. J. Vasc. Endovasc. Surg.*, **28** (2004), 484–493. https://doi.org/10.1016/j.ejvs.2004.05.012

30. M. H. Meissner, G. Moneta, K. Burnand, P. Gloviczki, J. M. Lohr, F. Lurie, et al., The hemodynamics and diagnosis of venous disease, *J. Vasc. Surg.*, **46** (2007), S4–S24. https://doi.org/10.1016/j.jvs.2007.09.043

31. X. Zhang, Z. Chen, Y. Liu, *The Material Point Method: A Continuum Based Particle Method for Extreme Loading Cases*, Academic Press, 2017.

32. J. Tan, W. Keller, S. Sohrabi, J. Yang, Y. Liu, Characterization of nanoparticle dispersion in red blood cell suspension by the lattice Boltzmann-immersed boundary method, *Nanomaterials*, **6** (2016), 30. https://doi.org/10.3390/nano6020030

33. D. D'Humières, Multiple–relaxation–time lattice Boltzmann models in three dimensions, *Philos. Trans. R. Soc. London, Ser. A*, **360** (2002), 437–451. https://doi.org/10.1098/rsta.2001.0955

34. Z. L. Guo, C. G. Zheng, B. C. Shi, Non-equilibrium extrapolation method for velocity and pressure boundary conditions in the lattice Boltzmann method, *Chin. Phys.*, **11** (2002), 366–374. https://doi.org/10.1088/1009-1963/11/4/310

35. C. S. Peskin, Flow patterns around heart valves: A numerical method, *J. Comput. Phys.*, **10** (1972), 252–271. https://doi.org/10.1016/0021-9991(72)90065-4

36. C. S. Peskin, The immersed boundary method, *Acta Numer.*, **11** (2002), 479–517. https://doi.org/10.1017/S0962492902000077

37. R. Mittal, G. Iaccarino, Immersed boundary methods, *Annu. Rev. Fluid Mech.*, **37** (2005), 239–261. https://doi.org/10.1146/annurev.fluid.37.061903.175743

38. F. B. Tian, L. Wang, Numerical modeling of sperm swimming, *Fluids*, **6** (2021), 73. https://doi.org/10.3390/fluids6020073

39. J. Ma, Y. Mei, Q. Liu, S. Peng, F. B. Tian, A front-tracking immersed boundary method for dynamics of three-dimensional capsules in multiphase flow systems involving viscoelastic fluids, *Phys. Fluids*, **37** (2025), 121905. https://doi.org/10.1063/5.0301629

40. N. Widdup, L. Wang, J. Young, F. B. Tian, The aerodynamic and acoustic performance of a bumblebee-inspired micro-air vehicle in Martian atmosphere, *Phys. Fluids*, **37** (2025), 091916. https://doi.org/10.1063/5.0288043

41. Z. Hao, B. Yin, M. Xu, G. Yang, A high-efficiency sharp-interface immersed boundary method based on multi-linear interpolation, *Phys. Fluids*, **36** (2024), 093617. https://doi.org/10.1063/5.0228369

42. S. Huang, D. Guo, J. Song, Y. Wang, G. Yang, B. Yin, Effect of bending kinematics for caudal fin on swimming performance with varying undulation wavelengths, *Ocean Eng.*, **311** (2024), 118907. https://doi.org/10.1016/j.oceaneng.2024.118907

43. D. Goldstein, R. Handler, L. Sirovich, Modeling a no-slip flow boundary with an external force field, *J. Comput. Phys.*, **105** (1993), 354–366. https://doi.org/10.1006/jcph.1993.1081

44. S. G. Bardenhagen, E. M. Kober, The generalized interpolation material point method, *Comp. Model. Eng. Sci.*, **5** (2004), 477–496. https://doi.org/10.3970/cmes.2004.005.477

45. D. Han, G. R. Liu, S. Abdallah, An Eulerian-Lagrangian-Lagrangian method for 2D fluid-structure interaction problem with a thin flexible structure immersed in fluids, *Comput. Struct.*, **228** (2020), 106179. https://doi.org/10.1016/j.compstruc.2019.106179

46. B. E. Griffith, N. A. Patankar, Immersed methods for fluid–structure interaction, *Annu. Rev. Fluid Mech.*, **52** (2020), 421–448. https://doi.org/10.1146/annurev-fluid-010719-060228

47. R. Pandey, M. Kumar, J. Majdoubi, M. Rahimi-Gorji, V. K. Srivastav, A review study on blood in human coronary artery: Numerical approach, *Comput. Methods Programs Biomed.*, **187** (2020), 105243. https://doi.org/10.1016/j.cmpb.2019.105243

48. B. T. Chan, E. Lim, K. H. Chee, N. A. A. Osman, Review on CFD simulation in heart with dilated cardiomyopathy and myocardial infarction, *Comput. Biol. Med.*, **43** (2013), 377–385. https://doi.org/10.1016/j.compbiomed.2013.01.013

49. L. Tikhomolova, Y. Gataulin, A. Yukhnev, D. Rosukhovskiy, Fluid–structure interaction modelling of the venous valve with elastic leaflets, *J. Phys. Conf. Ser.* , **1697** (2020), 012041. https://doi.org/10.1088/1742-6596/1697/1/012041

50. K. Lebahn, J. Keiler, W. Schmidt, J. Schubert, M. Reumann, A. Wree, et al., Mechanical characterization of the human femoral vein wall and its valves, *J. Mech. Behav. Biomed. Mater.*, **165** (2025), 106938. https://doi.org/10.1016/j.jmbbm.2025.106938

51. S. N. Doost, D. Ghista, B. Su, L. Zhong, Y. S. Morsi, Heart blood flow simulation: a perspective review, *Biomed. Eng. Online*, **15** (2016), 101. https://doi.org/10.1186/s12938-016-0224-8

52. J. Cisonni, A. D. Lucey, N. S. Elliott, M. Heil, The stability of a flexible cantilever in viscous channel flow, *J. Sound Vib.*, **396** (2017), 186–202. https://doi.org/10.1016/j.jsv.2017.02.045

53. X. Wang, I. C. Christov, Reduced modelling and global instability of finite-Reynolds-number flow in compliant rectangular channels, *J. Fluid Mech.*, **950** (2022), A26. https://doi.org/10.1017/jfm.2022.802

54. W. X. Huang, H. J. Sung, Three-dimensional simulation of a flapping flag in a uniform flow, *J. Fluid Mech.*, **653** (2010), 301–336. https://doi.org/10.1017/S0022112010000248

55. D. Kim, J. Cossé, C. H. Cerdeira, M. Gharib, Flapping dynamics of an inverted flag, *J. Fluid Mech.*, **736** (2013), R1. https://doi.org/10.1017/jfm.2013.555

56. C. Tang, N. S. Liu, X. Y. Lu, Dynamics of an inverted flexible plate in a uniform flow, *Phys. Fluids*, **27** (2015), 073601. https://doi.org/10.1063/1.4923281

57. F. B. Tian, H. Luo, L. Zhu, X. Y. Lu, Coupling modes of three filaments in side-by-side arrangement, *Phys. Fluids*, **23** (2011), 111903. https://doi.org/10.1063/1.3659892

58. B. S. Connell, D. K. Yue, Flapping dynamics of a flag in a uniform stream, *J. Fluid Mech.*, **581** (2007), 33–67. https://doi.org/10.1017/S0022112007005307

59. S. Mittal, S. Singh, Vortex-induced vibrations at subcritical *Re*, *J. Fluid Mech.*, **534** (2005), 185–194. https://doi.org/10.1017/S0022112005004635

60. F. B. Tian, Role of mass on the stability of flag/flags in uniform flow, *Appl. Phys. Lett.*, **103** (2013), 034101. https://doi.org/10.1063/1.4813006

61. C. Carallo, C. Tripolino, M. S. D. Franceschi, C. Irace, X. Y. Xu, A. Gnasso, Carotid endothelial shear stress reduction with aging is associated with plaque development in twelve years, *Atherosclerosis*, **251** (2016), 63–69. https://doi.org/10.1016/j.atherosclerosis.2016.05.048

62. A. Sanyal, H. Han, Artery buckling affects the mechanical stress in atherosclerotic plaques, *Biomed. Eng. Online*, **14** (2015), S4. https://doi.org/10.1186/1475-925X-14-S1-S4

63. K. V. Stoka, J. A. Maedeker, L. Bennett, S. A. Bhayani, W. S. Gardner, J. D. Procknow, et al., Effects of increased arterial stiffness on atherosclerotic plaque amounts, *J. Biomech. Eng.*, **140** (2018), 051007. https://doi.org/10.1115/1.4039175

64. C. M. Warboys, N. Amini, A. D. Luca, P. C. Evans, The role of blood flow in determining the sites of atherosclerotic plaques, *F1000 Med. Rep.*, **3** (2011), 5. https://doi.org/10.3410/m3-5

65. M. Mudau, A. Genis, A. Lochner, H. Strijdom, Endothelial dysfunction: the early predictor of atherosclerosis, *Cardiovasc. J. Afr.*, **23** (2012), 222–231. https://doi.org/10.5830/cvja-2011-068

66. S. Shaikh, J. Brittenden, R. Lahiri, P. A. Brown, F. Thiès, H. M. Wilson, Macrophage subtypes in symptomatic carotid artery and femoral artery plaques, *Eur. J. Vasc. Endovasc. Surg.*, **44** (2012), 491–497. https://doi.org/10.1016/j.ejvs.2012.08.005

67. N. Kumar, A. Khader, R. M. Pai, S. Khan, P. A. Kyriacou, Fluid structure interaction study of stenosed carotid artery considering the effects of blood pressure, *Int. J. Eng. Sci.*, **154** (2020), 103341. https://doi.org/10.1016/j.ijengsci.2020.103341

68. P. M. McGah, D. F. Leotta, K. W. Beach, A. Aliseda, Effects of wall distensibility in hemodynamic simulations of an arteriovenous fistula, *Biomech. Model. Mechanobiol.*, **13** (2013), 679–695. https://doi.org/10.1007/s10237-013-0527-7

69. C. Dupont, A. Salsac, D. Barthès-Biesel, M. Vidrascu, P. L. Tallec, Influence of bending resistance on the dynamics of a spherical capsule in shear flow, *Phys. Fluids*, **27** (2015), 051902. https://doi.org/10.1063/1.4921247

70. K. Shoele, R. Mittal, Flutter instability of a thin flexible plate in a channel, *J. Fluid Mech.*, **786** (2016), 29–46. https://doi.org/10.1017/jfm.2015.632

71. E. Konstantinidis, C. Liang, Dynamic response of a turbulent cylinder wake to sinusoidal inflow perturbations across the vortex lock-on range, *Phys. Fluids*, **23** (2011), 075102. https://doi.org/10.1063/1.3592330

72. R. C. Kloosterziel, P. Orlandi, G. F. Carnevale, Saturation of equatorial inertial instability, *J. Fluid Mech.*, **767** (2015), 562–594. https://doi.org/10.1017/jfm.2015.63

73. L. Zhu, C. S. Peskin, Interaction of two flapping filaments in a flowing soap film, *Phys. Fluids*, **15** (2003), 1954–1960. https://doi.org/10.1063/1.1582476

74. F. M. White, J. Majdalani, *Viscous Fluid Flow*, McGraw-Hill New York, 2006.

75. G. H. Ding, B. H. Ma, J. J. Deng, W. Z. Yuan, K. Liu, Accurate measurements of wall shear stress on a plate with elliptic leading edge, *Sensors*, **18** (2018), 2682. https://doi.org/10.3390/s18082682

76. Y. Chen, Y. Xiong, W. Jiang, F. Yan, M. Guo, Q. Wang, et al., Numerical simulation on the effects of drug eluting stents at different Reynolds numbers on hemodynamic and drug concentration distribution, *Biomed. Eng. Online*, **14** (2015), S16. https://doi.org/10.1186/1475-925X-14-S1-S16

77. F. B. Tian, H. Luo, L. Zhu, J. C. Liao, X. Y. Lu, An efficient immersed boundary-lattice Boltzmann method for the hydrodynamic interaction of elastic filaments, *J. Comput. Phys.*, **230** (2011), 7266–7283. https://doi.org/10.1016/j.jcp.2011.05.028

AIMS Press